

Article

# Mesostructure and Magnetic Properties of SiO<sub>2</sub>-Co Granular Film on Silicon Substrate

Natalia A. Grigoryeva<sup>1,\*</sup> , Victor Ukleev<sup>2</sup> , Alexey A. Vorobiev<sup>3</sup> , Alexander I. Stognij<sup>4</sup>, Nikolay N. Novitskii<sup>4</sup>, Leonid V. Lutsev<sup>5</sup> and Sergey V. Grigoriev<sup>6</sup><sup>1</sup> Department of Physics, Saint-Petersburg State University, 198504 St. Petersburg, Russia<sup>2</sup> Laboratory for Neutron Scattering and Imaging, Paul Scherrer Institute, CH-5232 Villigen, Switzerland<sup>3</sup> Department of Physics and Astronomy, Uppsala University, 75120 Uppsala, Sweden<sup>4</sup> Scientific and Practical Materials Research Center of the National Academy of Sciences of Belarus, BY-220072 Minsk, Belarus<sup>5</sup> Ioffe Physical-Technical Institute of Russian Academy of Sciences, 194021 St. Petersburg, Russia<sup>6</sup> Petersburg Nuclear Physics Institute NRC “Kurchatov Institute”, Gatchina, 188300 St. Petersburg, Russia

\* Correspondence: n.a.grigorieva@yandex.ru

**Abstract:** Granular films SiO<sub>2</sub>(Co) exhibit unusual magnetic and magnetotransport properties which are strongly dependent on the composition of the film and material of a substrate. For example, the injection magnetoresistance (IMR) coefficient reaches a giant (GIMR) value of 10<sup>5</sup>% at room temperature in SiO<sub>2</sub>(Co) films on an n-GaAs substrate. However, the IMR effect is negligible in the case of a similar granular film deposited on the n-Si substrate. In this report, the structural and magnetic properties of granular film SiO<sub>2</sub>(Co) on Si substrate are studied with the aim to understand the cause of the difference in IMR coefficients for SiO<sub>2</sub>(Co) thin film deposited on n-GaAs and on n-Si substrates. Investigations were carried out using complementary methods of Polarized Neutron Reflectometry, Grazing Incidence Small-Angle X-ray Scattering, X-ray Reflectometry, Scanning Electron Microscope, and SQUID magnetometry. It is shown that the interface layer between the granular film and Si substrate exhibits metallic rather than magnetic properties and eliminates the GIMR effect. This interface layer is associated with the Si diffusion to Co nanoparticles and the formation of the metallic cobalt silicides.

**Keywords:** granular film; nanoparticles; grazing-incidence small-angle X-ray scattering; polarized neutron reflectometry

**PACS:** 75.70.Cn; 75.75.-c; 75.50.Lk



**Citation:** Grigoryeva, N.A.; Ukleev, V.; Vorobiev, A.A.; Stognij, A.I.; Novitskii, N.N.; Lutsev, L.V.; Grigoriev, S.V. Mesostructure and Magnetic Properties of SiO<sub>2</sub>-Co Granular Film on Silicon Substrate. *Magnetochemistry* **2022**, *8*, 167.

<https://doi.org/10.3390/magnetochemistry8120167>

Academic Editors: Cătălin-Daniel Constantinescu and Lucian Petrescu

Received: 25 September 2022

Accepted: 15 November 2022

Published: 24 November 2022

**Publisher's Note:** MDPI stays neutral with regard to jurisdictional claims in published maps and institutional affiliations.



**Copyright:** © 2022 by the authors. Licensee MDPI, Basel, Switzerland. This article is an open access article distributed under the terms and conditions of the Creative Commons Attribution (CC BY) license (<https://creativecommons.org/licenses/by/4.0/>).

## 1. Introduction

Granular films (GFs) are nanocomposites that consist of metallic magnetic nanoparticles incorporated in an insulating matrix. GFs with a very well-controlled nanostructure have promising technological applications in microwave devices, spintronics, medicine and biology [1–7]. Structural investigations of GFs play a crucial role and often facilitates the interpretation of their electrical and magnetic properties as well as their interconnection. A complex interplay of intrinsic properties can be caught through their structural features also accounting for finite-size effects, size distribution, surface effects, and nanoparticle interactions.

The effect of giant injection magnetoresistance (GIMR) has been observed in the GFs SiO<sub>2</sub>(x at.% Co) deposited on GaAs substrate [8,9]. The GIMR phenomenon is a magnetic-field-induced suppression of the spin-polarized electron current from the GF into the semiconductor substrate. The IMR coefficient has maximum values for structures with Co concentrations in the range 54 ÷ 75 at.%. In the case of the opposite current direction (electrons drift from the semiconductor into the granular film) the magnetoresistance effect

becomes less pronounced. The GIMR coefficient reaches  $10^5$  % in a narrow temperature range  $240 \text{ K} < T < 300 \text{ K}$  at the magnetic field of  $H = 10 \text{ kOe}$  applied in the sample plane and at the voltage  $U = 70 \text{ V}$  applied perpendicular to the sample plane.

The extreme value of this effect at room temperature and the possibility of controlling the resistivity of heterostructure by varying the magnetic field could be used in the development of spintronic devices such as spin injectors, spin diodes, and transistors. Unlike crystalline silicon, the gallium arsenide substrate has a number of disadvantages in practical use: it is mechanically fragile and thermally unstable above  $600 \text{ }^\circ\text{C}$  due to As evaporation, which imposes restrictions on the synthesis technology. The use of silicon substrates would eliminate these problems and provide additional advantages, such as its intrinsic carrier concentration being  $n_i = 1.02 \times 10^{10} \text{ cm}^{-3}$  and the energy gap being  $E_g = 1.12 \text{ eV}$  (compared to GaAs –  $n_i = 2.1 \times 10^6 \text{ cm}^{-3}$  and  $E_g = 1.43 \text{ eV}$ , respectively). However, while the GIMR effect reaches  $10^5$  % in the case of the GF deposited on GaAs substrate, the GIMR is negligible in the case of a similar granular film deposited on n-Si substrate [8], and the intrinsic magnetoresistance of  $\text{SiO}_2(x \text{ at.}\% \text{ Co})/\text{Si}$  films has even negative values. In the present work we studied  $\text{Au}/\text{SiO}_2(\text{Co } x \text{ at.}\%)/\text{Si}$  heterostructures with cobalt content of  $x = 54, 60, 70, 75, 82 \text{ at.}\%$ . The aim of the study is to investigate the structural features and the associated magnetic properties of the heterostructures  $\text{Au}/\text{GF}/\text{Si}$  and to reveal the role of Si substrate in the negligible GIMR effect. For this purpose, we used the Polarized Neutron Reflectometry (PNR) technique, which we combined with complementary techniques of Grazing Incidence Small Angle X-ray Scattering (GISAXS), X-ray Reflectometry (XRR), Scanning Electron Microscope (SEM), and Superconducting Quantum Interference Device Magnetometry (SQUID).

The paper is organized in the following way. Section 2 gives details of the sample preparation and experimental results obtained via different methods to reveal structural and magnetic properties. Section 3 provides a discussion and interpretation of the results combined. A combination of different methods makes it possible to build a model explaining the negligible value of the GIMR effect, providing that almost all structural and magnetic properties of GF are practically the same for the films disposed on GaAs and Si substrates. It is shown that the interface layer between the GF and Si substrate shows metallic rather than magnetic properties and eliminates the GIMR effect. This interface layer is associated with the Si diffusion to Co nanoparticles and the formation of metallic cobalt silicides. Section 4 is the conclusion.

## 2. Experiment

### 2.1. Sample Preparation

The granular films  $\text{SiO}_2(x \text{ at.}\% \text{ Co})$  were synthesized by ion beam co-sputtering [10,11] of the composite cobalt-quartz target on the commercial n-Si substrate heated to  $200 \text{ }^\circ\text{C}$  and misoriented by 2 degrees from (100) plane to (110) plane and with the thickness of 0.4 mm. The resistivity of the Si substrate was measured by the dc four-probe method at room temperature and was equal to  $3.7 \text{ } \Omega \cdot \text{cm}$ . The concentration of cobalt nanoparticles in  $\text{SiO}_2$  was set by the ratio of cobalt and quartz target areas. The film was capped by 2 nm of the gold layer as a conductive contact for magnetoresistance measurements. The sputtering method and choice of components are described in ref. [12]. A detailed description of the characteristics of granular films is given in ref. [8].

The granular films  $\text{SiO}_2(x \text{ at.}\% \text{ Co})$  can be differentiated by their conductivity into three classes depending on the Co concentration.

- (1) Class of GFs ( $\text{SiO}_2(x \text{ at.}\% \text{ Co})$ ), at  $x < 40 \text{ at.}\%$  shows dielectric properties since isolated metal particles are dispersed in a dielectric continuum.
- (2) Class of GFs ( $\text{SiO}_2(x \text{ at.}\% \text{ Co})$ ), at  $40 \text{ at.}\% \leq x \leq 85 \text{ at.}\%$  demonstrates semiconductor-like (intermediate) properties as metal particles with an increase in  $x$  become interconnected to form a maze structure. The electrical conductivity in this regime is due to percolation along the metallic maze and electron tunneling between isolated metal

particles. The concentration of Co  $x \approx 40$  at.% is a percolation threshold, below which only the tunneling process contributes to the conductivity of the granular metal.

- (3) Class of GFs ( $\text{SiO}_2(x \text{ at.}\% \text{ Co})$ ), at  $x > 85$  at.% can be attributed to metals as the volume fraction of the metal  $x$  is large, metal grains merge and form a metallic continuum with dielectric inclusions.

For this study, the granular films  $\text{SiO}_2(x \text{ at.}\% \text{ Co})$  with Co concentrations of  $x = 54, 60, 70, 75, 82$  at.% deposited on Si substrate were chosen. A total of 5 batches of  $\text{SiO}_2(x \text{ at.}\% \text{ Co})/\text{Si}$  heterostructures with the same concentrations were synthesized and studied to ensure the repeatability of synthesis results. Figure 1 demonstrates SEM images for  $\text{SiO}_2(54 \text{ at.}\% \text{ Co})/\text{Si}$  (a), and for  $\text{SiO}_2(82 \text{ at.}\% \text{ Co})/\text{Si}$  (b). Field Emission SEM (FE-SEM) Zeiss Leo 1530 capable of 2.5 nanometer resolution equipped with an In-Lens secondary electron detector has been used. The average size of cobalt nanoparticles has been obtained from a set of linear measurements using ImageJ software and equals about  $75 \pm 15$  Å. The microscope achieves a resolution of approx. 1 nm.

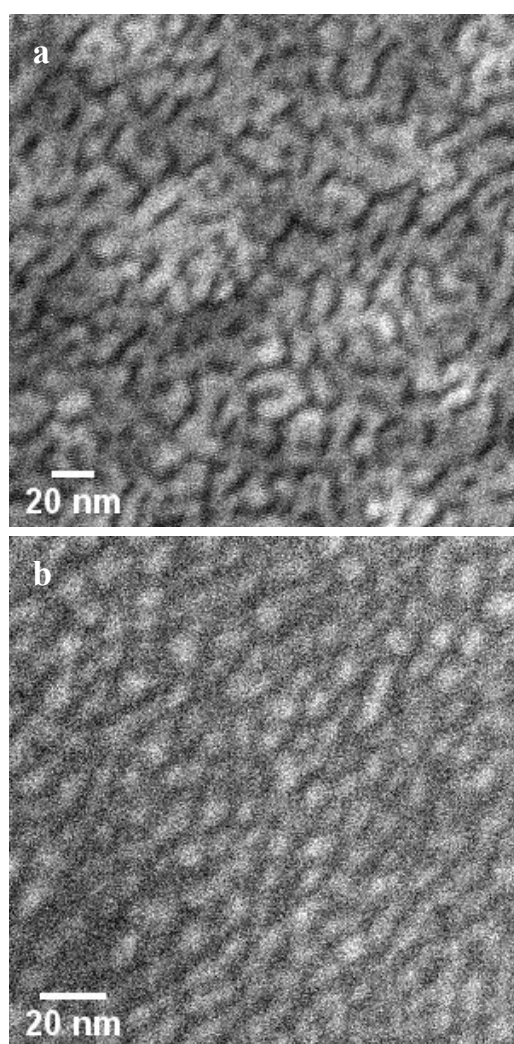


**Figure 1.**  $\text{SiO}_2(54 \text{ at.}\% \text{ Co})/\text{Si}$  (a) and  $\text{SiO}_2(82 \text{ at.}\% \text{ Co})/\text{Si}$  (b) images in the secondary electron mode with the InLens detector, mounted above the films. Light contrast corresponds to the  $\text{SiO}_2$  matrix and dark areas correspond to Co inclusions.

## 2.2. Grazing Incidence Small Angle X-ray Scattering and X-ray Reflectometry

The Grazing Incidence Small Angle X-ray Scattering (GISAXS) and X-ray Reflectometry (XRR) experiments were carried out at ID10 beamline of European Synchrotron Radiation Facility (ESRF, Grenoble, France) [13]. The geometry of the GISAXS (Figure 2) is described

by the grazing incidence angle  $\alpha_i$  and two scattering angles  $\alpha_f$  (out of sample plane) and  $\varphi$  (in-plane). Information on the electron density distribution in the  $z$  direction is obtained by measuring the scattering intensity as a function of the momentum transfer component  $Q_z$  perpendicular to the sample plane. Meanwhile, the lateral structure of the granular film, its surface and its interface with the silicon substrate can be studied by measuring intensity as a function of the component  $Q_y$  lying in the sample plane. A detailed description of the theory and methodology of the GISAXS technique can be found in the review [14–16]. The GISAXS experiment with the GF  $\text{SiO}_2$ (x at.% Co) on GaAs substrate can be found in [17]. The collimated X-ray beam of the size  $1 \times 0.1 \text{ mm}^2$  and wavelength  $\lambda = 0.95 \text{ \AA}$ , impinging the sample surface at the grazing angle  $\alpha_i = 0.32^\circ$ , was used for the GISAXS experiment. The scattering patterns were recorded with the two-dimensional position-sensitive detector MARCCD-133. The central part of the detector was protected from high-intensity direct and specular beams by a lead absorber.

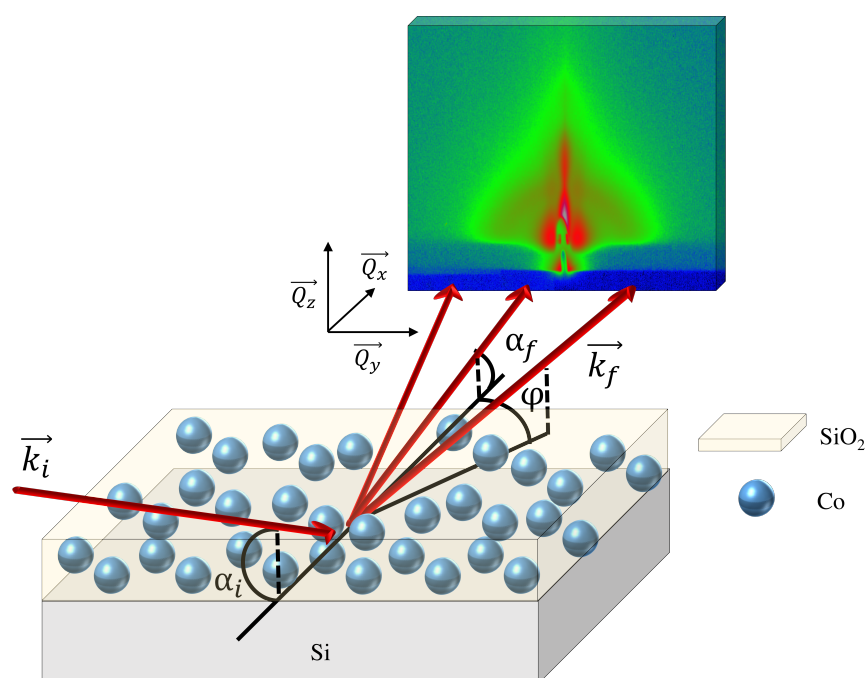


**Figure 2.** Geometry of the GISAXS experiment:  $\mathbf{k}_i$  and  $\mathbf{k}_f$  are the wave vectors of the incident and scattered beams, respectively;  $\alpha_i$ ,  $\alpha_f$  and  $\varphi$  angles determine the momentum transfer components  $Q_x$ ,  $Q_y$ ,  $Q_z$ .

The two-dimensional GISAXS intensity maps from the samples Au/GF/Si are shown in Figure 3a–c. Several features can be distinguished. Firstly, the presence of a broad elliptical diffuse halo whose intensity is increased at  $\alpha_f = \alpha_c = 0.25^\circ$  (where  $\alpha_c$  is the critical angle of the Total External Reflection) due to the Yoneda anomalous scattering and has zero intensity at  $\alpha_f = 0$ , i.e., below the sample horizon. This broad elliptical diffuse halo is a typical manifestation of scattering from an isotropic three-dimensional system of scatterers (cobalt nanoparticles) located at a distance  $l_1 = 2\pi/Q_1$  from each other, where  $Q_1$  expressed in momentum transfer units is the radius of the diffuse halo.

The second feature of the scattering pattern is the presence of two symmetrical peaks at angles  $\varphi = \pm 0.29^\circ$ . Such peaks correspond to the scattering from the nanoparticles spatially arranged within the monolayer at the interface with the substrate [14–16,18]. By taking the peaks coordinate  $Q_2$  it is easy to calculate the average interparticle distance at the interface:  $l_2 = 2\pi/Q_2$ . To determine both  $l_1$  and  $l_2$  distances the cuts along  $\varphi$  direction of the two-dimensional intensity maps at  $\alpha_f = 0.25^\circ$  were taken (Figure 3d).

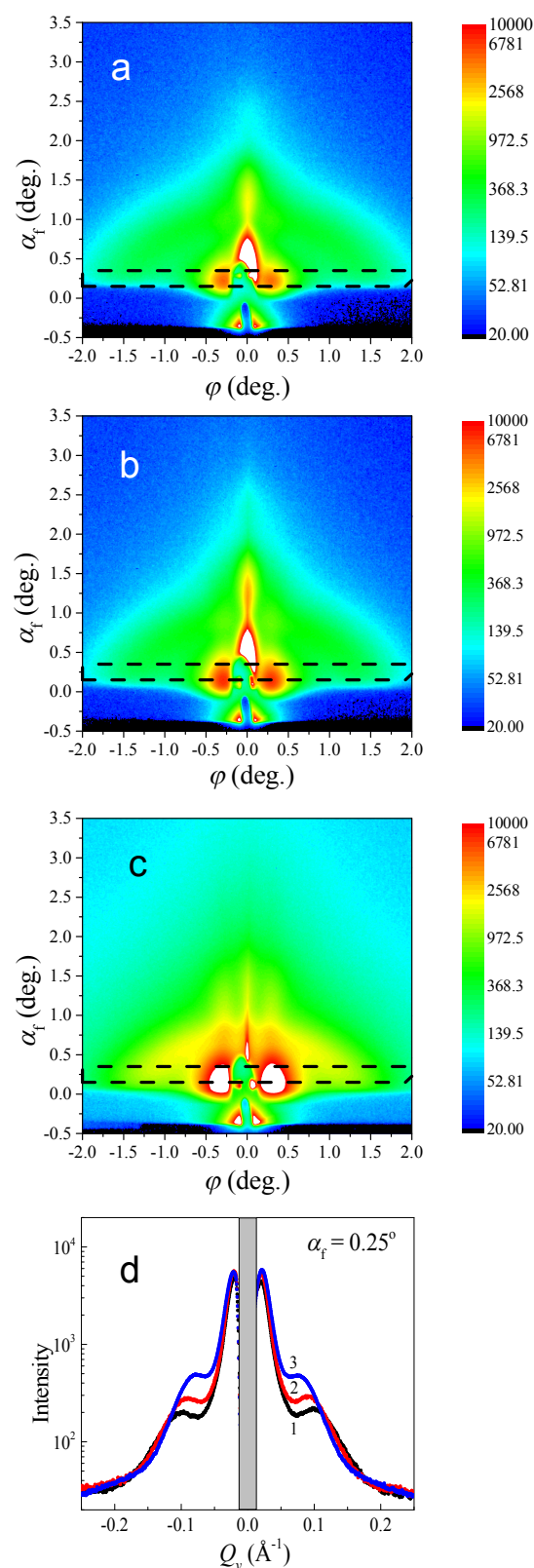


**Figure 3.** (a) The two-dimensional GISAXS intensity maps from the samples SiO<sub>2</sub>(38 at.% Co)/Si (a), SiO<sub>2</sub>(54 at.% Co)/Si (b), and SiO<sub>2</sub>(82 at.% Co)/Si (c). The dashed horizontal lines indicate the integration regions for the one-dimensional profiles shown on (d) panel. (d) The scattering intensity profiles along  $\phi$  direction at  $\alpha_f = 0.25^\circ$  for SiO<sub>2</sub>(38 at.% Co)/Si—curve 1, SiO<sub>2</sub>(54 at.% Co)/Si—curve 2, and SiO<sub>2</sub>(82 at.% Co)/Si—curve 3. The gray area corresponds to the beamstop shadow.

In XRR experiments, the intensity of X-rays scattered in the direction  $\alpha_i = \alpha_f$  and  $\varphi = 0$  was measured as a function of the incidence angle  $\alpha_i$ . The measurements were performed with a  $1 \times 0.1 \text{ mm}^2$  beam with a wavelength of  $1.56 \text{ \AA}$ . To detect the reflected beam, we used an mBraun-50M linear position-sensitive detector, which made it possible not only to measure the desired signal but also to simultaneously determine the background, which was then subtracted. The specular reflection curve  $R(Q_z)$  thus obtained is related to the one-dimensional in-depth distribution of the electron density of the sample  $\rho(z)$  using the Parratt method [19]. The results of the XRR experiment are presented in Figure 4, where the intensity of the reflected beam is shown as a function of the momentum transfer for Au/SiO<sub>2</sub>(60 at.% Co)/Si and Au/SiO<sub>2</sub>(82 at.% Co)/Si.

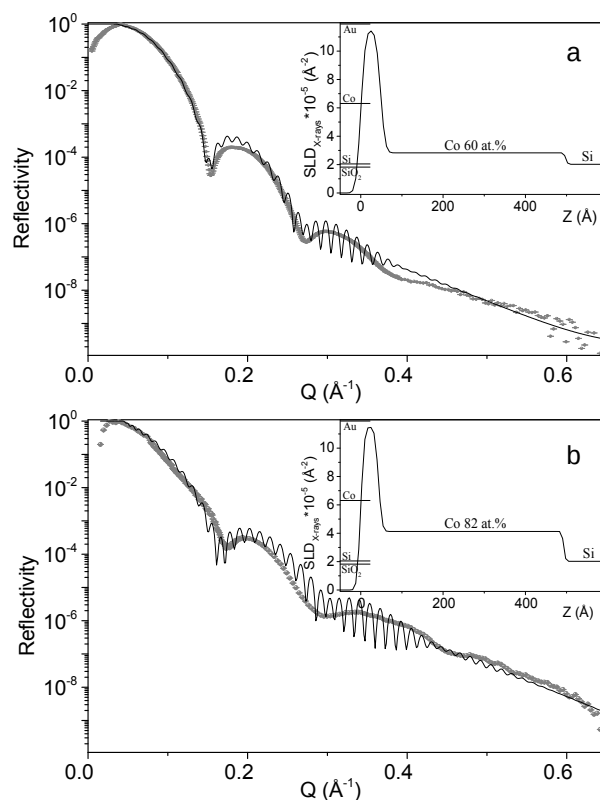


**Figure 4.** Synchrotron X-ray reflectometry from Au/SiO<sub>2</sub> (60 at.% Co)/Si (a) and Au/SiO<sub>2</sub> (82 at.% Co)/Si (b) heterostructures. The gray points are experimental data, the solid line is the theoretical curve corresponding to the model of the electron-density distribution shown in the inset with the indication of electron densities plotted for the pure components of the sample.

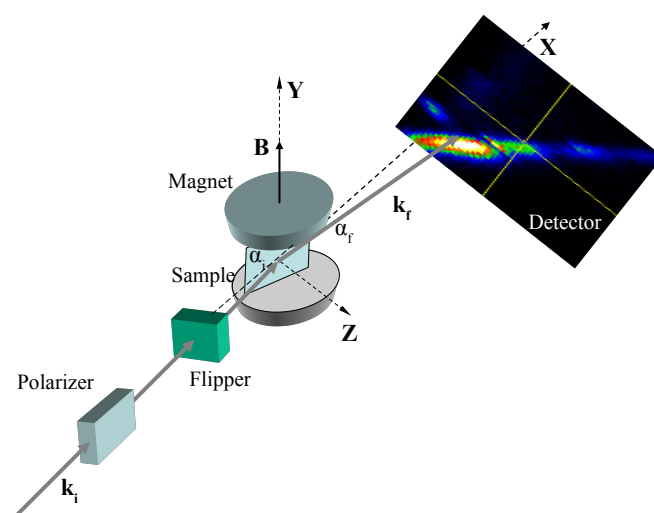
The experimental reflectivity data shows clear maxima with oscillating intensity (Kiessig fringes) caused by the finite thickness of the film. The experimental curves (Figure 4) are sufficiently well reproduced by the model containing two layers on a substrate Si. The parameters of the model include the depth profile of the electron scattering length density ( $SLD_{X\text{-rays}}$ ), layer thickness ( $d$ ) and interface (or surface) roughness ( $\sigma$ ). The first layer corresponds to the technical layer of gold, the second layer corresponds to the granular SiO<sub>2</sub>( $x$  at.%Co) film with a thickness of  $450 \text{ \AA}$ . The fitting parameters for each layer adjusted to minimize the value of reduced  $\chi^2$ —a weighted measure of goodness of fit are presented in Table 1. The absence of fast oscillations corresponding to the total thickness of the bilayer Au/GF cannot be explained by the insufficient resolution of the instrument. Measurements were taken at a step of  $0.02$  degrees ( $50$  steps/ $1$  degree). This is enough to resolve a film with a thickness of about  $450 \text{ \AA}$  (the oscillation period from  $450 \text{ \AA}$  is  $0.1$  degrees). The reduction in the oscillation amplitude can be attributed to the interface roughness or, rather, to smeared  $SLD_{X\text{-rays}}$  contrast (a contrast of the electron density) between a granular film and a substrate.

**Table 1.** Parameters of the model used to approximate the experimental X-ray reflectometry curves.

Layer	d (Å)	SLD <sub>X-rays</sub> · 10 <sup>-5</sup> (Å <sup>-2</sup> )	σ (Å)
Au/SiO <sub>2</sub> (60 at.% Co)/Si			
Au	48 ± 2	11.5 ± 0.1	9.0 ± 0.2
Granular film	450 ± 2	2.83 ± 0.05	9.0 ± 0.2
Si	–	2.024 ± 0.05	3.8 ± 0.2
Au/SiO <sub>2</sub> (82 at.% Co)/Si			
Au	43 ± 2	11.5 ± 0.1	7.0 ± 0.3
Granular film	450 ± 2	4.13 ± 0.05	7.0 ± 0.3
Si	–	2.024 ± 0.05	3.6 ± 0.2

### 2.3. Polarized Neutron Reflectometry

A detailed description of the polarized neutron reflectometry technique can be found elsewhere [20]. The experiment was carried out at the SuperADAM reflectometer at Institut Laue-Langevin (Grenoble, France) [21–23]. Typical geometry of the PNR experiment is shown in Figure 5.

**Figure 5.** Typical geometry of the polarized neutron reflectometry experiment.

We exploited a neutron beam with the wavelength  $\lambda = 4.41 \text{ \AA}$  and the initial polarization  $P_0 = 0.98$ . The lateral components of neutron momentum transfer  $Q_x$  and  $Q_y$  were equal to zero, and the vertical component  $Q_z$  was equal to  $4\pi\sin(\alpha_f)/\lambda$ , where  $\alpha_f$  is the angle of the scattered beam with wave vector  $\mathbf{k}_f$ . Intensities of the reflected beams with initial polarization  $+P_0$  and  $-P_0$ , i.e., along and against the direction of the external magnetic field  $\mathbf{B}$ , were measured one by one. The magnetic field from 0 to 320 mT was applied parallel to the film surface and perpendicular to the incident neutron beam with wave vector  $\mathbf{k}_i$ . The direction of  $\mathbf{P}_0$  with respect to  $\mathbf{B}$  was switched by a spin Flipper. Specularly reflected neutrons were detected by the  $^3\text{He}$  position-sensitive detector. Measurements were performed at temperatures, where the GIMR effect is not detected ( $T = 120 \text{ K}$ ), reaches its maximum ( $T = 300 \text{ K}$ ) and again is not detected ( $T = 420 \text{ K}$ ) [8]. The data for every temperature were taken after the demagnetization process. No difference between reflectivity curves  $R(Q_z, +P_0)$  and  $R(Q_z, -P_0)$  was observed at  $B = 0 \text{ mT}$ , while the application of the external field resulted in a pronounced splitting of two components (Figure 6).

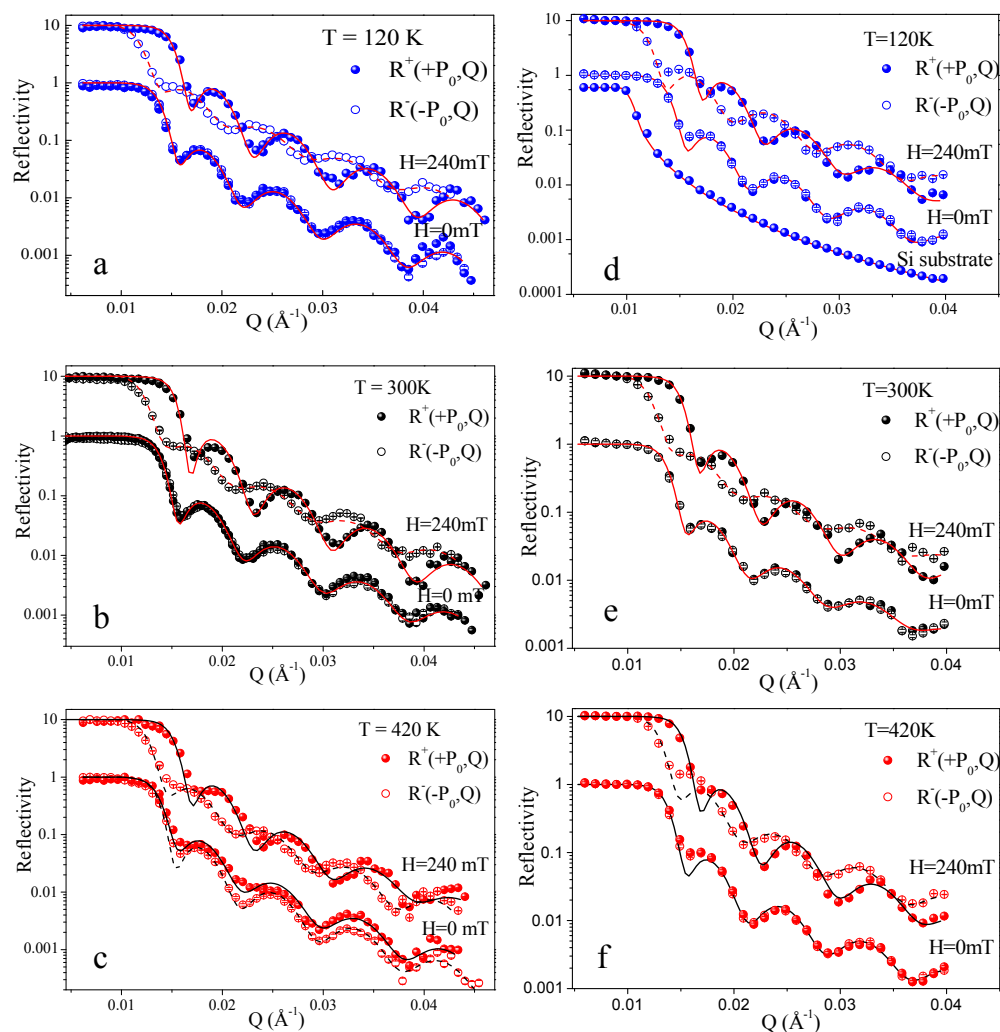


**Figure 6.** The experimental (symbols) and fitted model (lines) reflectivity curves for the samples Au/SiO<sub>2</sub>(60 at.% Co)/Si (a–c) and Au/SiO<sub>2</sub>(70 at.% Co)/Si (d–f) at fields  $B = 0$  and  $B = 240$  mT for  $T = 120$  K (a,d), 300 K (b,e), and 420 K (c,f). Measured and fitted model curves at  $B = 240$  mT are multiplied by 10 for convenience.

For fitting the Polarized Neutron Reflectometry experimental data the Parratt algorithm was used [19]. The following parameters were included in the fitting routine: the beam width, the sample length, the resolution, the background and the detector offset. The scattering length density (SLD) profile (Figure 7) represents the distribution of the scattering potential of the sample into the depth of the film (in  $Z$  direction Figure 5). The results for all studied samples are shown to coincide qualitatively with insignificant numerical variations associated with the concentration of cobalt in the granular film (Figure 7). All PNR curves at different temperatures and  $B$  were fitted with the same structural parameters: thickness ( $d$ ), roughness ( $\sigma$ ), and nuclear scattering length density ( $N_n$ ). The magnetic scattering length density ( $N_m$ ), which depends on the applied magnetic field, varied in the corresponding datasets (Tables 2 and 3).

From Figure 7, it is clear that a good quantitative agreement between model calculations and experimental data has been achieved. The difference in the granular film thickness,  $d$ , defined by PNR and XRR methods is related to different batches of samples.

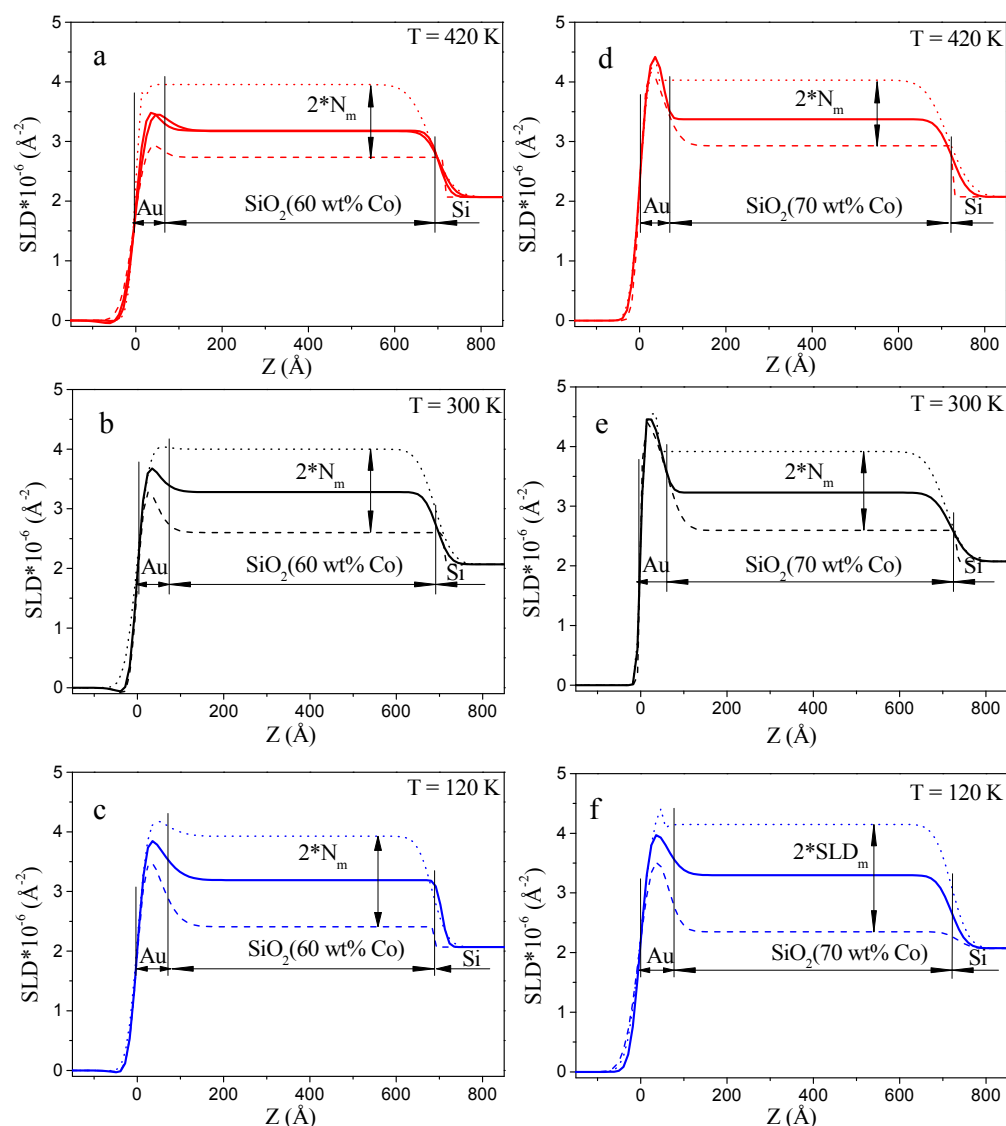


**Figure 7.** The SLD profiles  $\rho^+$  (dot line) and  $\rho^-$  (dashed line) of the samples Au/SiO<sub>2</sub> (60 at.% Co)/Si (a–c) and Au/SiO<sub>2</sub> (70 at.% Co)/Si (d–f) at  $B = 240$  mT for  $T = 420$  K (a,c), 300 K (b,e), and 120 K (c,f). The solid line corresponds to the SLD profile at  $H = 0$  T for every polarization of neutrons.

**Table 2.** Parameters of the model used to approximate the PNR curves for Au/SiO<sub>2</sub> (60 at.% Co)/Si.

Layer	d (Å)	$N_n \cdot 10^{-6}$ (Å <sup>-2</sup> )	$N_m \cdot 10^{-7}$ (Å <sup>-2</sup> )	H (mT)	$\sigma$ (Å)
T = 120 K					
Au	45 ± 2	3.8 ± 0.2	–	0	11.0 ± 1.0
			0.33 ± 0.02	20	
			1.71 ± 0.02	40	
			3.25 ± 0.02	60	
GF	680 ± 2	3.29 ± 0.03	3.91 ± 0.02	100	10.0 ± 1.0
			5.02 ± 0.02	240	
			7.66 ± 0.02	320	
Si	–	2.073 ± 0.02	–	–	40 ± 2

Table 2. Cont.

Layer	d (Å)	$N_n \cdot 10^{-6}$ (Å <sup>-2</sup> )	$N_m \cdot 10^{-7}$ (Å <sup>-2</sup> )	H (mT)	$\sigma$ (Å)
T = 300 K					
Au	45 ± 2	3.7 ± 0.2	–	0	11.0 ± 1.0
			0.13 ± 0.02	20	
			0.99 ± 0.02	40	
			1.83 ± 0.02	60	
GF	680 ± 2	3.29 ± 0.03	2.52 ± 0.02	100	10.0 ± 1.0
			3.62 ± 0.02	240	
			6.48 ± 0.02	320	
Si		2.073 ± 0.02	–		50 ± 2
T = 420 K					
Au	45 ± 2	3.5 ± 0.2	–	0	11.0 ± 1.0
			0.05 ± 0.02	20	
			1.10 ± 0.02	40	
			1.49 ± 0.02	60	
GF	680 ± 2	3.38 ± 0.03	2.21 ± 0.02	100	10.0 ± 1.0
			2.99 ± 0.02	240	
			5.05 ± 0.02	320	
Si		2.073 ± 0.02	–		50 ± 2

Table 3. Parameters of the model used to approximate the PNR curves for Au/SiO<sub>2</sub> (70 at.% Co)/Si.

Layer	d (Å)	$N_n \cdot 10^{-6}$ (Å <sup>-2</sup> )	$N_m \cdot 10^{-7}$ (Å <sup>-2</sup> )	H (mT)	$\sigma$ (Å)
T = 120 K					
Au	45 ± 2	4.0 ± 0.2	–	0	11.0 ± 1.0
			0.06 ± 0.02	20	
			3.01 ± 0.02	40	
			4.37 ± 0.02	60	
GF	685 ± 2	3.29 ± 0.03	5.13 ± 0.02	100	10.0 ± 1.0
			6.53 ± 0.02	240	
			8.26 ± 0.02	320	
Si		2.073 ± 0.02	–		50 ± 2
T = 300 K					
Au	45 ± 2	3.7 ± 0.2	–	0	11.0 ± 1.0
			0.04 ± 0.02	20	
			0.65 ± 0.02	40	
			1.28 ± 0.02	60	
GF	685 ± 2	3.29 ± 0.03	1.92 ± 0.02	100	10.0 ± 1.0
			2.87 ± 0.02	240	
			5.70 ± 0.02	320	
Si		2.073 ± 0.02	–		50 ± 2
T = 420 K					
Au	45 ± 2	3.5 ± 0.2	–	0	11.0 ± 1.0
			0.00 ± 0.02	20	
			0.005 ± 0.02	40	
			0.02 ± 0.02	60	
GF	685 ± 2	3.29 ± 0.03	0.35 ± 0.02	100	10.0 ± 1.0
			1.39 ± 0.02	240	
			3.64 ± 0.02	320	
Si		2.073 ± 0.02	–		50 ± 2

### 2.4. SQUID Magnetometry

Static magnetic properties of the samples were characterized by SQUID magnetometry (Quantum Design MPMS-5S) at the Institute of Condensed Matter Physics (Braunschweig, Germany). The magnetization curves  $M(H)$  were recorded up to 5 T. The magnetic field was applied parallel to the plane of the film. As an example,  $M(H)$  of the sample  $\text{SiO}_2$  (75 at.% Co)/Si taken at  $T = 200$  K and 300 K are shown in Figure 8 after subtraction of the diamagnetic contribution of the Si substrate and the  $\text{SiO}_2$  matrix. A shift of the magnetic hysteresis loops along the field axis and a change of the coercive field as a function of temperature are observed. (insert (a) in Figure 8). In the fields region of  $0.8 \div 1.8$  T there are specific hysteresis loops—“pockets” (inserts (b,c) in Figure 8).

The actual magnetic saturation value of the films is quite difficult to detect using SQUID techniques because the overall high-field signal includes the dominant diamagnetic contribution of the substrate, appearing due to its relatively large volume. If the granular film itself shows a small linear response in the high field regions, this is convoluted with an overwhelming diamagnetic signal and it is challenging to reliably subtract the latter contribution in order to separate the magnetic properties of the nanolayer itself. The saturation magnetization value of the  $\text{SiO}_2(\text{Co})$  film obtained by SQUID magnetometry (Figure 8)  $M_s \approx 60 \text{ emu/cm}^3$  differs significantly from the saturation magnetization of bulk cobalt  $M_{\text{Co}} = 1422 \text{ emu/cm}^3$ .

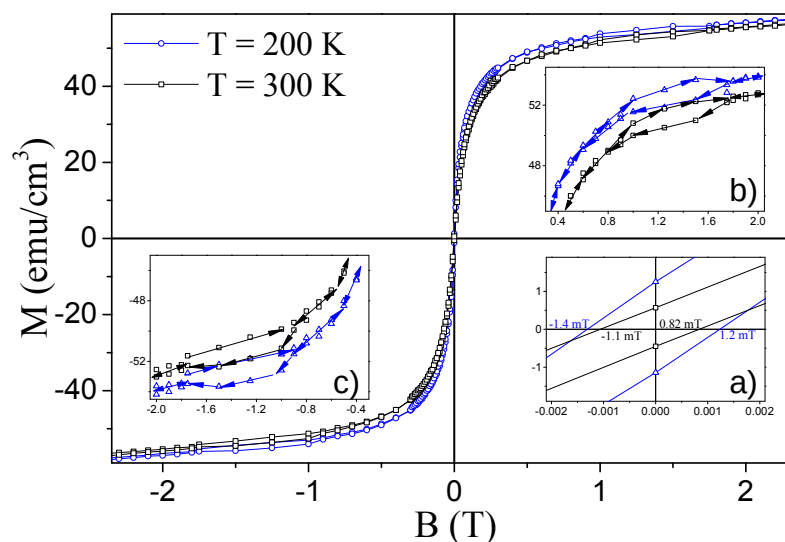


**Figure 8.** Magnetic field dependence of the  $\text{SiO}_2$  (75 at.% Co)/Si sample magnetization at magnetic field from  $-5$  T to  $5$  T. Inserts: (a)—region of the coercive fields, (b,c)—regions of the specific hysteresis loops.

### 3. Discussion

The GISAXS data from the samples Au/GF/Si has clearly shown two nanoparticle subsystems in GFs with different average interparticle distances  $l_1$  and  $l_2$  (Figure 3). The interparticle distance  $l_1$  for the first subsystem increases with the increasing cobalt concentration:  $64 \pm 2 \text{ \AA}$  for  $\text{SiO}_2$  (38 at.% Co)/Si,  $70 \pm 2 \text{ \AA}$  for  $\text{SiO}_2$ (54 at.% Co)/Si, and  $88 \pm 2 \text{ \AA}$  for  $\text{SiO}_2$  (82 at.% Co)/Si (Figure 3d). It is clear that the determined interparticle distance  $l_1$  for these concentrations of Co should be equal to the size of nanoparticles because of the percolation limit. As one can see, the value of  $l_1$  obtained by GISAXS is in good agreement with the particle size observed by SEM on the top surface of the GF, where percolation is clearly visible (Figure 1).

In contrast, the second subsystem with a characteristic distance  $l_2 = 300 \text{ nm}$  is not revealed by SEM measurements. This is due to the fact that it is most likely located at the burred GF/Si interface. A similar structure containing two subsystems of nanoparticles in the granular films  $\text{SiO}_2$  (x at.% Co) deposited on GaAs substrate was observed in [17,24].

There it was shown that the specific interface layer of cobalt nanoparticles is formed between the GF and GaAs substrate with an in-plane interparticle distance  $\sim 320 \text{ \AA}$  and the thickness  $\sim 70 \text{ \AA}$  [17,24].

The formation of such a specific layer on the GF/Semiconductor interface may be caused by a number of reasons. The deposition of cobalt on a substrate at the initial stage leads to the clustering of a thin cobalt film due to the dynamics of Co on Si, or GaAs [25–28]. The activation energy for clustering was found to be  $0.3 \pm 0.2 \text{ eV}$  [25], indicating that a Co surface diffusion process dominates the kinetics. The surface energy of cobalt is about  $2500\text{--}2900 \text{ erg/cm}^2$ , while the surface energy of silicon corresponds to  $1230 \text{ erg/cm}^2$  for the (111) plane,  $1510 \text{ erg/cm}^2$  for the (110) plane, and  $2130 \text{ erg/cm}^2$  for the plane (100). The surface energy of GaAs is  $860 \text{ erg/cm}^2$  [29,30]. Another reason for the formation of a specific layer at the interface is presumably related to the process of heteroepitaxial growth of the GF by ion beam co-sputtering directly onto a semiconductor substrate, while the next layers are grown in the homoepitaxial regime [31].

However, the X-ray and Polarized neutron reflectometry data (Figures 4, 6 and 7) do not confirm the coexistence of two nanoparticle subsystems in GFs, or they are not sensitive enough to the existence of a specific layer at the GF/Semiconductor interface in  $\text{SiO}_2$  (x at.% Co)/Si samples. In contrast to the GISAXS results, the film model which fits the XRR and PNR data in the best way consists of only two layers on the Si substrate: a granular film layer and the capping Au layer, i.e., there is no specific layer on the GF/Semiconductor interface. Why do the PNR method, which is highly sensitive to changes in magnetic properties, and the XRR method, which is highly sensitive to changes in electron density contrast, fail to detect an interface layer?

The next question deals with the study and interpretation of the magnetic properties of the granular films. The magnetic scattering length density  $N_m$  has the opposite sign for neutrons with initial polarization  $+\mathbf{P}_0$  and  $-\mathbf{P}_0$  (along and against  $\mathbf{B}$ ) and its value is directly proportional to the magnetization component  $\mathbf{M}$  parallel to  $\mathbf{B}$ :

$$M = \left( \frac{m_n \mu_n}{2\pi \hbar^2} \right)^{-1} \frac{N_m}{4\pi}, \quad (1)$$

where  $m_n$  and  $\mu_n$  are the mass and magnetic moment of the neutron. Comparing SLD profiles  $\rho^+ = N_n + N_m$  and  $\rho^- = N_n - N_m$  corresponding to  $R(Q_z, +\mathbf{P}_0)$  and  $R(Q_z, -\mathbf{P}_0)$ , respectively, one can obtain a value of the magnetization in every layer forming the sample film.

From the non-zero values of  $N_m$  at the SLD profiles (Figure 7) one can conclude that only GF is magnetized under the applied field and tends to saturate the magnetic moment at  $B \geq 300 \text{ mT}$ . Magnetizations of the GF in  $\text{SiO}_2$ (60 at.% Co)/Si and  $\text{SiO}_2$  (70 at.% Co)/Si samples calculated from  $N_m$  according to Equation (1) are presented in Figure 9 as a function of the applied magnetic field for  $T = 120, 300$  and  $420 \text{ K}$ . In Figure 9, the magnetic SLD  $N_m$  is normalized to magnetic SLD of bulk cobalt  $N_m(\text{Co}) = 4.24 \times 10^{-6} \text{ \AA}^{-2}$ . From Figure 9, it follows that the GF is in the ferromagnetic state at all three temperatures. Its magnetization decreases with increasing temperature: at the maximum applied field  $B = 320 \text{ mT}$  we found that  $N_m/N_m(\text{Co}) = 0.21$  at  $T = 120 \text{ K}$  while decreasing down to  $0.17$  at  $T = 300 \text{ K}$  and to  $0.14$  at  $T = 420 \text{ K}$  for  $\text{SiO}_2$  (60 at.% Co) and decreasing down to  $0.14$  at  $T = 300 \text{ K}$  and to  $0.09$  at  $T = 420 \text{ K}$  for  $\text{SiO}_2$  (70 at.% Co). Why is the magnetization, determined by the PNR method so much smaller than the magnetization of bulk Co? It is smaller by a factor of 5 to 10 at different temperatures.

Let us analyze the nuclear scattering length densities of neutrons and X-rays for all samples in order to answer these questions. The fit parameters in PNR and XRR models show excellent agreement between the measured and expected nuclear SLD values of Si ( $2.073 \times 10^{-6} \text{ \AA}^{-2}$  and  $2.024 \times 10^{-5} \text{ \AA}^{-2}$ , respectively). The fits of the nuclear SLD values of Au in the PNR and the XRR experiments are slightly lower than the expected bulk values ( $4.5 \times 10^{-6} \text{ \AA}^{-2}$  and  $12.47 \times 10^{-5} \text{ \AA}^{-2}$ , respectively). The reason could be the discontinuous layer of gold since its thickness is below  $50 \text{ \AA}$ . A number of studies

demonstrate changes in the physical and chemical properties of thin gold films associated with their island structure [32–34].

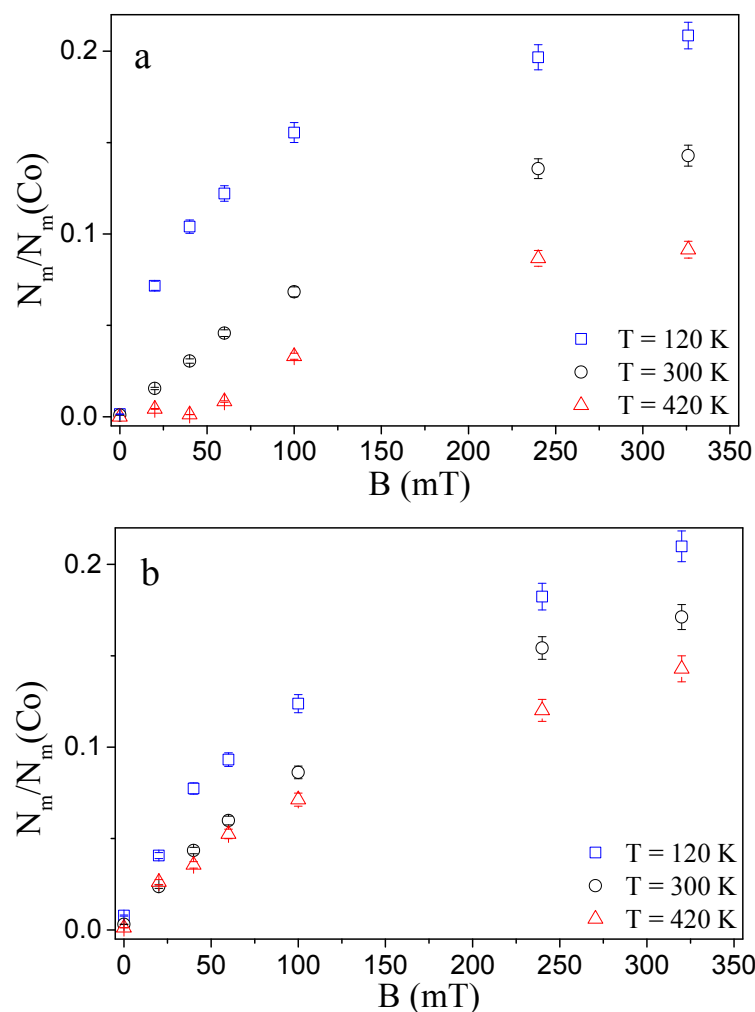


**Figure 9.** Magnetic field dependence of fitted magnetic SLD value  $N_m$  normalized to magnetic SLD of bulk cobalt  $N_m(\text{Co})$  for the ferromagnetic films  $\text{SiO}_2$  (70 at.% Co) (a) and  $\text{SiO}_2$  (60 at.% Co) (b).

The measured nuclear SLD of the GF layer is substantially higher for neutrons and lower for X-rays as compared to expected values (Tables 1–4). Table 4 shows the calculated  $N_n$  and  $\text{SLD}_{\text{X-ray}}$  values for a given ratio of Co/ $\text{SiO}_2$  in GF under the assumption that cobalt can interact with oxygen from the silicon oxide dielectric matrix or oxidize in air. Unfortunately, there is no reliable way to determine the thickness of the oxide layer on the surface of cobalt nanoparticles in the present study. It is obvious that the cobalt grains must be partially oxidized for the nuclear SLD to be higher for neutrons or lower for X-rays, compared to the values for a given ratio of Co/ $\text{SiO}_2$  in GF. All cobalt oxides are antiferromagnets, in contrast to pure cobalt (Table 5). Magnetization measurements (Figure 8) reveal that for  $\text{SiO}_2(x \text{ at.\%Co})/\text{Si}$  heterostructures exchange biasing of the magnetic hysteresis loop along the field axis is observed. The exchange bias describes a phenomenon associated with interfacial coupling between ferromagnetic and antiferromagnetic materials [35]. In our investigation, the exchange biasing of the magnetic hysteresis loop confirms the oxidation of cobalt nanoparticles. The exchange biasing field, like the coercive field, changes as a function of temperature and is about 10 percent of the coercive field (insert (a) in Figure 8).

Another small but well-distinguished feature of the magnetization curve is the small hysteretic pockets in the field range from 0.8 to 1.6 T. They are well-detected both in the positive and negative halves of the magnetization curve. They were also detected for GF on the GaAs substrate [36]. An interesting feature of this hysteresis loop is counterintuitive

large values of the magnetization when the field increases and smaller magnetization values when the field decreases. This feature can be referred to as the same biasing phenomenon of the Co (ferromagnetic) particles with the oxidized (antiferromagnetic) surface, to the so-called "core-shell" model. In this case, the magnetization of the Co particle is responsible for the large ferromagnetic response of the GF system, while the antiferromagnetic shell may show a spin flop in a certain field range, which may be energetically more favorable than the collinear spin arrangement. Considering its really small (4% only) contribution imposed on the top of the magnetization curve, we point out the biased (ferro-antiferro) magnetic nature of this phenomenon but do not go into any further details.

**Table 4.** The calculated  $N_n$  and  $SLD_{X\text{-rays}}$  values for a given ratio of Co/SiO<sub>2</sub> in GF under the assumption that cobalt can be oxidized.

Ratio xCo/(1-x)SiO <sub>2</sub>	xCo		xCoO		xCo <sub>2</sub> O <sub>3</sub>	
	$N_n, 10^{-6} \text{ \AA}^{-2}$	$SLD_{X\text{-rays}}, 10^{-5} \text{ \AA}^{-2}$	$N_n, 10^{-6} \text{ \AA}^{-2}$	$SLD_{X\text{-rays}}, 10^{-5} \text{ \AA}^{-2}$	$N_n, 10^{-6} \text{ \AA}^{-2}$	$SLD_{X\text{-rays}}, 10^{-5} \text{ \AA}^{-2}$
0.38/0.62	3.0	3.56	3.77	2.97	3.74	2.64
0.54/0.46	2.81	4.27	3.91	3.44	3.86	2.97
0.60/0.40	2.74	4.54	3.95	3.6	3.90	3.1
0.70/0.30	2.62	4.98	4.04	3.9	3.98	3.4
0.75/0.25	2.55	5.22	4.08	4.05	4.01	3.38
0.82/0.18	2.47	5.51	4.14	4.24	4.08	3.52

**Table 5.** The calculated  $N_n$  and  $SLD_{X\text{-rays}}$  values are given with Density (D), Molecular weight (MW) and Number of molecules per  $\text{\AA}^3$  (n) for compounds (Comp) that may be formed in the granular film, or at the interfaces.

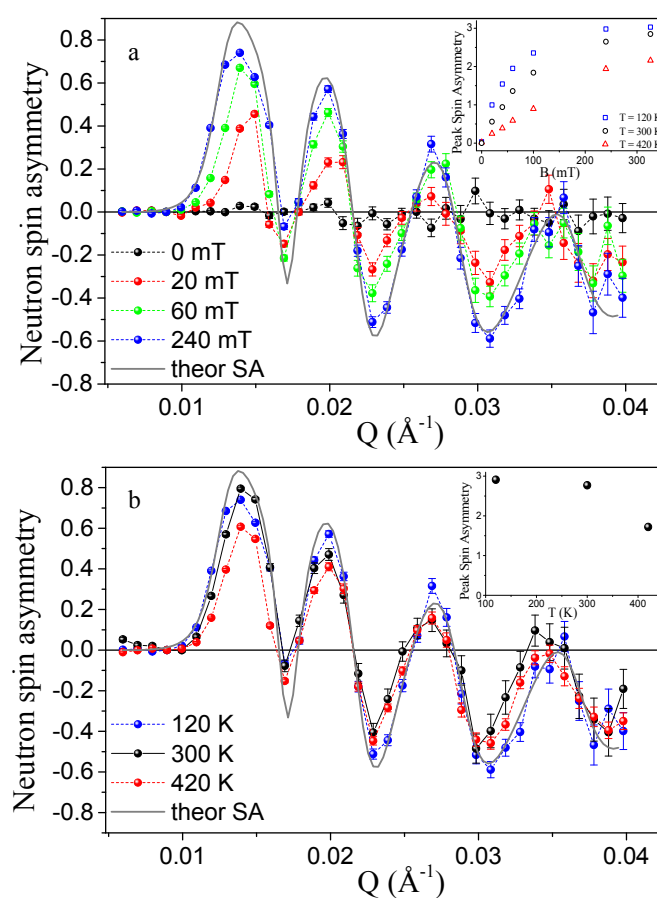
Comp	D, g/ccm	MW, g/mole	n	$N_n, 10^{-6} \text{ \AA}^{-2}$	$SLD_{X\text{-rays}}, 10^{-5} \text{ \AA}^{-2}$	Type of Magnetism at T = 300 K	Type of Conductivity at T = 300 K
Au	19.3	196.97	0.059	4.5	12.47	diamagnetic	metal
SiO <sub>2</sub>	2.2	60.08	0.022	3.46	1.88	diamagnetic	insulator
CoO	6.45	74.93	0.0518	4.29	4.77	antiferromagnetic	semiconductor
Co <sub>2</sub> O <sub>3</sub>	5.18	165.86	0.0188	4.2	3.88	antiferromagnetic	semiconductor
Co <sub>3</sub> O <sub>4</sub>	6.073	240.80	0.0152	4.66	4.53	antiferromagnetic	semiconductor
Co	8.9	58.933	0.091	2.26	6.3	ferromagnetic	metal
CoSi	6.3	87.02	0.0436	2.88	4.77	diamagnetic	semimetal
Co <sub>2</sub> Si	7.1	145.95	0.0293	2.67	5.23	diamagnetic	metal
CoSi <sub>2</sub>	5.3	115.10	0.0277	2.97	4.15	diamagnetic	metal
Si	2.33	28.086	0.05	2.074	2.024	diamagnetic	semiconductor

Figure 10 demonstrates the neutron spin asymmetry calculated by:

$$SA = \frac{R(Q_z, +\mathbf{P}_0) - R(Q_z, -\mathbf{P}_0)}{R(Q_z, +\mathbf{P}_0) + R(Q_z, -\mathbf{P}_0)} \quad (2)$$

As the neutron spin asymmetry is a very reliable method to study the intrinsic nano-magnetic features [37,38], it provides direct evidence that these magnetic properties originate from the composite thin film region and the substrate and surface play no detectable role. The spin asymmetry is purely related to the local magnetic moment in the sample and characterizes the in-depth distribution of the magnetization in GF directly. The observed peak SA occurs at  $Q_z = 0.0136 \pm 0.004 \text{ \AA}^{-1}$  and exceeds 80% (Figure 10a), which competes with that of standard magnetic alloys [39] and is large compared to the spin asymmetries typical of dilute magnetic systems [40]. The magnetic moment of the sample proportional to the SA peak area increases with the applied external field and saturates at the experimental field of  $240 \div 320 \text{ mT}$  (insert in Figure 10a). In contrast to SQUID

magnetometry, PNR is unaffected by complications of diamagnetic or weak paramagnetic responses because they produce very low magnetizations per volume. Instead, the PNR signal is dominated by scattering effects from large local net magnetization, typically caused by a well-aligned collinear spin structure. Consequently, the small value of the neutron spin asymmetry at low fields (insert in Figure 10a) confirms the traits noted in the hysteresis from the SQUID data (Figure 8)—a low remanence and a low coercive field ( $B_c < 1.4$  mT) which are attributed to either superparamagnetic behavior or a wandering anisotropy axis. This shows that, without a sufficient applied field, the magnetic moments in GF do not stay well aligned in any specific direction. The possible reason for this is that there are inhomogeneous magnetically ordered patches in the GF layer that experience a distribution of local spin anisotropies and consequently have a distribution of magnetization angles that are only co-aligned in a magnetic field and relax under zero field. In addition, the magnetic moment in GF changes moderately with temperature (insert in Figure 10b), indicating a strong magnetic exchange coupling.



**Figure 10.** The neutron spin asymmetry, SA, for Au/SiO<sub>2</sub> (70 at.% Co)/Si fitted (gray line) to the chemical and magnetic model previously described in the text (Figure 7): (a)—under applied magnetic fields up to 320 mT, (b)—for different temperatures at B = 240 mT. Insert in panel (a)—the field-dependence of the integral intensity of the peak spin asymmetry for different temperatures. Insert in panel (b)—the temperature dependence of the integral intensity of the peak spin asymmetry at B = 240 mT. For clarity, data for (a) at B = 40, 100, and 320 mT are omitted.

As it is shown in Figure 10, the SA changes its sign upon the increase in the momentum transfer  $Q_z$ . We interpret this observation as the presence of the "magnetically dead" layer in the GF at its interface with the Si substrate. The thickness of this layer is difficult to determine exactly, but it should be of the order of (1/10) of the thickness of the granular film itself. A similar effect of the magnetically dead layers in the PNR was observed in the multilayered structures (see, for example, [41,42].)

Based on the above, it should be assumed that the oxidation of cobalt nanoparticles is the reason for such a low magnetization value of the granular film with cobalt concentrations from 54 at.% to 82 at.% compared to pure cobalt. The same difference of the magnetic SLD value normalized to magnetic SLD of bulk cobalt was observed for GF deposited on GaAs substrate in [43].

The answer to the question of why the highly sensitive PNR and XRR methods fail to detect an interface layer between GF and Si substrate will also allow us to answer the main question of this article: what is the reason for the dramatic difference in IMR coefficients for identical  $\text{SiO}_2(x \text{ at.}\% \text{ Co})$  granular films deposited on GaAs, or Si substrates.

It was noted above that Co due to the higher surface free energy as compared to Si would tend to grow as islands at the beginning of the deposition. The phase composition and magnetic properties of cobalt films deposited on the silicon substrate were studied in [36]. It was shown that as the film thickness increases, an interface cobalt silicide and an island film of a solid solution of silicon in cobalt are successively formed. The growth of metallic cobalt begins only after the deposition of a Co layer with a thickness of more than 7 Å. The calculated  $N_n$  values are given in Table 5 for chemical compounds that may be formed in the granular film, or at the interfaces due to boundary interlayer diffusion leading to the formation of an interface of variable binary composition—cobalt silicides. Table 5 shows that cobalt silicides and cobalt oxides have similar  $\text{SLD}_{\text{X-rays}}$  values, which does not allow the GF and an additional interface layer to be distinguished in the Z direction (Figure 2) by XRR experiments. Wherein in the Y direction (Figure 2), an additional interface layer with large periodicity  $l_2 = 300 \pm 10 \text{ Å}$  is detectable by GISAXS due to the high contrast of  $\text{SLD}_{\text{X-rays}}$  between the multiphase cobalt granules and the  $\text{SiO}_2$ . Thus, both the XRR and PNR experimental results are well described by the model of a uniform granular cobalt film with a noticeably oxidized surface of the granules and a high surface roughness at the interface with the silicon substrate.

Increasing the silicon concentration to 30% in the Co-Si solid solution makes the large cobalt granules practically non-magnetic due to the charge transfer effect. Moreover, due to the formation of cobalt silicide at the GF/Si interface, the conductivity of the granular film will be determined by the chains "granule (Co)-metal (Co-Si)-semiconductor (Si)", and not by electron tunneling between ferromagnetic granules through the  $\text{SiO}_2$  dielectric matrix into the Si semiconductor. This leads to a strong decrease in the magnetoresistive coefficient to a few percent in  $\text{SiO}_2(x \text{ at.}\% \text{ Co})$  heterostructures on a Si substrate compared to the really giant IMR value in  $\text{SiO}_2(71 \text{ at.}\% \text{ Co})$  on a GaAs substrate [8].

#### 4. Conclusions

In the present paper, we studied the structure and magnetic properties of the maze structure with interconnected cobalt particles  $\text{SiO}_2(x \text{ at.}\% \text{ Co})$  deposited on Si substrate at  $54 \text{ at.}\% \leq x \leq 82 \text{ at.}\%$ . Investigations were carried out using Polarized Neutron Reflectometry, Grazing Incidence Small Angle X-ray Scattering, X-ray Reflectometry, Scanning Electron Microscopy, and Superconducting Quantum Interference Device Magnetometry.

The reason for the dramatic difference in IMR coefficients for  $\text{SiO}_2(x \text{ at.}\% \text{ Co})$  heterostructures deposited on GaAs or Si substrates was established. Despite the fact that both granular films have very similar values for thickness, interparticle distances, and magnetizations, as well as the additional layer of Co at the interface granular film/substrate, there is a difference in the interface morphology for  $\text{SiO}_2(x \text{ at.}\% \text{ Co})/\text{Si}$ . On the interface granular film/Si substrate there is boundary interlayer diffusion of Si atoms into Co, leading to the formation of an interface of variable binary composition - cobalt silicides. The formation of cobalt silicide at the GF/Si interface leads to the conductivity of the granular film determined by the electron movement via chains "ferromagnetic granule (Co)-metal (Co-Si)-semiconductor (Si)", and not by the electron tunneling between ferromagnetic granules through the  $\text{SiO}_2$  dielectric matrix into the Si semiconductor. A high value of the GIMR effect in  $\text{SiO}_2(x \text{ at.}\% \text{ Co})$  on GaAs [8,44] substrate is probably related to the spin-dependent potential barrier formed in the accumulation electron layer in the

semiconductor near the interface. The action of the spin-dependent potential barrier is amplified by the avalanche process and by the electron accumulation in the quantum well in the semiconductor interface region induced by the backscattering process of injected electrons on exchange-split levels [44]. In the granular film SiO<sub>2</sub> (x at.% Co) on the Si substrate, the cobalt silicide does not allow the formation of the region at the GF/Si interface saturated with electrons capable of polarizing in the direction of the applied magnetic field. Therefore, further efforts to form a quantum well with exchange-split levels on the well top at the surface of Si are necessary to gain a high positive magnetoresistance in SiO<sub>2</sub> (x at.% Co)/Si heterostructure. For example, this can be achieved by introducing a buffer layer between the granular film and substrate [45,46].

**Author Contributions:** Conceptualization, N.A.G.; methodology, N.A.G.; validation, N.A.G. and S.V.G.; investigation, N.A.G., V.U., A.A.V.; resources, A.I.S., N.N.N. and L.V.L.; data curation, V.U. and A.A.V.; writing—original draft preparation, N.A.G. and V.U.; writing—review and editing, S.V.G.; visualization, A.A.V.; supervision, S.V.G.; project administration, L.V.L. All authors have read and agreed to the published version of the manuscript.

**Funding:** This work is financially supported by the Ministry of Science and Higher Education of the Russian Federation in the framework of Agreement No. 075-15-2022-830 (Prolongation of Agreement No. 075-15-2021-1358 from 12 October 2021).

**Institutional Review Board Statement:** Not applicable.

**Informed Consent Statement:** Not applicable.

**Data Availability Statement:** The data that support the findings of this study are available from the corresponding author upon reasonable request.

**Acknowledgments:** Authors would like to thank Institut Laue-Langevin, European Synchrotron Radiation Facility and Institute of Condensed Matter Physics of TU Braunschweig for the provided experimental opportunities. We would like to acknowledge M. Wolf, A. Mistonov and D. Menzel for the assistance with the neutron and magnetometry measurements. The authors are grateful to the staff of the Interdisciplinary Resource Center for Nanotechnology and the Center of X-ray diffraction studies at the Research park of Saint Petersburg State University for preliminary research of Au/SiO<sub>2</sub>(Co)/Si heterostructures, as well as Saint Petersburg State University for financial support (Activity 6—grant for academic mobility 2019, ID:41160111).

**Conflicts of Interest:** The authors declare that they have no conflict of interest.

## References

1. Gerber, A.; Milner, A.; Groisman, B.; Karpovsky, M.; Sulpice, A. Magnetoresistance of granular ferromagnet-insulator films. *Thin Solid Films* **1997**, *304*, 319–322. [[CrossRef](#)]
2. Stuart, H.R.; Hall, D.G. Island size effects in nanoparticle-enhanced photodetectors. *Appl. Phys. Lett.* **1998**, *73*, 3815–3817. [[CrossRef](#)]
3. Kodama, R. Magnetic Nanoparticle. *J. Magn. Magn. Mater.* **1999**, *200*, 359–372. [[CrossRef](#)]
4. Fujimori, H.; Ohnuma, S.; Kobayashi, N.; Masumoto, T. Spintronics in metal-insulator nanogranular magnetic thin films. *J. Magn. Magn. Mater.* **2006**, *304*, 32–35. [[CrossRef](#)]
5. Žutić, I.; Fabian, J.; Sarma, S.D. Spintronics: Fundamentals and applications. *Rev. Mod. Phys.* **2004**, *76*, 323.
6. Atwater, H.A.; Polman, A. Plasmonics for improved photovoltaic devices. *Nat. Mater.* **2010**, *9*, 205–213. [[CrossRef](#)]
7. Lambert, C.-H.; Mangin, S.; Varaprasad, B.C.S.; Takahashi, Y.; Hehn, M.; Cinchetti, M.; Malinowski, G.; Hono, K.; Fainman, Y.; Aeschlimann, M.; et al. All-optical control of ferromagnetic thin films and nanostructures. *Science* **2014**, *345*, 1337–1340. [[CrossRef](#)]
8. Lutsev, L.V.; Stognij, A.I.; Novitskii, N.N. Giant magnetoresistance in semiconductor/granular film heterostructures with cobalt nanoparticles. *Phys. Rev. B* **2009**, *80*, 184423. [[CrossRef](#)]
9. Lutsev, L. Potential barrier for spin-polarized electrons induced by the exchange interaction at the interface in the ferromagnet/semiconductor heterostructure. *J. Phys. Condens. Matter* **2006**, *18*, 5881. [[CrossRef](#)] [[PubMed](#)]
10. Miller, N.C.; Shirn, G.A. Co-sputtered Au-SiO<sub>2</sub> cermet films. *Appl. Phys. Lett.* **1967**, *10*, 86. [[CrossRef](#)]
11. Miller, N.C.; Hardiman, B.; Shirn, G.A. Transport properties, microstructure, and conduction model of cosputtered Au-SiO<sub>2</sub> cermet films. *J. Appl. Phys.* **1970**, *41*, 1850. [[CrossRef](#)]
12. Stognij, A.I.; Novitskii, N.N.; Stukalov, O.M. Separate cobalt-copper interface smoothing under the action of low-energy argon ion bombardment. *Tech. Phys. Lett.* **2003**, *29*, 43–46. [[CrossRef](#)]

13. Smilgies, D.M.; Boudet, N.; Struth, B.; Konovalov, O. Troika II: A versatile beamline for the study of liquid and solid interfaces. *J. Synchrotron Radiat.* **2005**, *12*, 329–339. [[CrossRef](#)]
14. Renaud, G.; Lazzari, R.; Leroy, F. Probing surface and interface morphology with Grazing Incidence Small Angle X-ray Scattering. *Surf. Sci. Rep.* **2009**, *64*, 255–380. [[CrossRef](#)]
15. Renaud, G.; Lazzari, R.; Revenant, C.; Barbier, A.; Noblet, M.; Ulrich, O.; Leroy, F.; Jupille, J.; Borensztein, Y.; Henry, C.R.; et al. Real-time monitoring of growing nanoparticles. *Science* **2003**, *300*, 1416–1419. [[CrossRef](#)] [[PubMed](#)]
16. Lazzari, R.; Renaud, G.; Revenant, C.; Jupille, J.; Borensztein, Y. Adhesion of growing nanoparticles at a glance: Surface differential reflectivity spectroscopy and grazing incidence small angle X-ray scattering. *Phys. Rev. B* **2009**, *79*, 125428. [[CrossRef](#)]
17. Grigoreva, N.; Vorobev, A.; Ukleev, V.; Dyadkina, E.; Lutsev, L.; Stognij, A.; Novitskii, N.; Grigorev, S. Investigation of the SiO<sub>2</sub>(Co)/GaAs heterostructures using the surface scattering of synchrotron radiation. *JETP Lett.* **2010**, *92*, 767–773. [[CrossRef](#)]
18. Schwartzkopf, M.; Buet, A.; Körstgens, V.; Metwalli, E.; Schlage, K.; Benecke, G.; Perlich, J.; Rawolle, M.; Rothkirch, A.; Heidmann, B.; et al. From atoms to layers: in situ gold cluster growth kinetics during sputter deposition. *Nanoscale* **2013**, *5*, 5053–5062. [[CrossRef](#)] [[PubMed](#)]
19. Parratt, L.G. Surface Studies of Solids by Total Reflection of X-rays. *Phys. Rev.* **1954**, *95*, 359. [[CrossRef](#)]
20. Ankner, J.; Felcher, G. Polarized-neutron reflectometry. *J. Magn. Magn. Mater.* **1999**, *200*, 741–754. [[CrossRef](#)]
21. Wolff, M.; Zhernenkov, K.; Zabel, H. Neutron reflectometry with ADAM at the ILL: Present status and future perspectives. *Thin Solid Films* **2007**, *515*, 5712–5715. [[CrossRef](#)]
22. Devishvili, A.; Zhernenkov, K.; Dennison, A.J.; Toperverg, B.; Wol, M.; Hjörvarsson, B.; Zabel, H. SuperADAM: Upgraded polarized neutron reflectometer at the Institut Laue-Langevin. *Rev. Sci. Instruments* **2013**, *84*, 025112. [[CrossRef](#)]
23. Vorobiev, A.; Devishvili, A.; Palsson, G.; Rundlöf, H.; Johansson, N.; Olsson, A.; Dennison, A.; Wolff, M.; Giroud, B.; Aguetaz, O.; et al. Recent upgrade of the polarized neutron reflectometer Super ADAM. *Neutron News* **2015**, *26*, 25–26. [[CrossRef](#)]
24. Ukleev, V.A.; Grigoryeva, N.A.; Dyadkina, E.A.; Vorobiev, A.A.; Lott, D.; Lutsev, L.V.; Stognij, A.I.; Novitskiy, N.N.; Mistonov, A.A.; Menzel, D.; et al. Magnetic properties of the SiO<sub>2</sub>(Co)/GaAs interface: Polarized neutron reflectometry and SQUID magnetometry. *Phys. Rev. B* **2012**, *86*, 134424. [[CrossRef](#)]
25. Ottavian, G.; Tu, K.N.; Psaras, P.; Nobili, C. In situ resistivity measurement of cobalt silicide formation. *J. Appl. Phys.* **1987**, *62*, 2290–2294. [[CrossRef](#)]
26. Cabral, C., Jr.; Barmak, K.; Gupta, J.; Clevenger, L.A.; Arcot, B.; Smith, D.A.; Harper, J.M.E. Role of stress relief in the hexagonal-clos-packed to face-centered-cubic phase transformation in cobalt thin films. *J. Vac. Sci. Technol.* **1993**, *A11*, 1435–1440. [[CrossRef](#)]
27. Colgan, E.G., Jr.; Cabral, C.; Kotecki, D.E. Activation energy for CoSi and CoSi<sub>2</sub> formation measured during rapid thermal annealing. *J. Appl. Phys.* **1995**, *77*, 614–619. [[CrossRef](#)]
28. Lowes, T.D.; Zinke-Allmang, M. Cobalt grain growth on clean Si(100) Surfaces. *Scanning Microsc.* **1998**, *12*, 119–129.
29. Jaccodine, R.J. Surface energy of germanium and silicon. *J. Electrochem. Soc.* **1963**, *110*, 524. [[CrossRef](#)]
30. Messmer, C.; Bilello, J.C. The surface energy of Si, GaAs, and GaP. *J. Appl. Phys.* **1981**, *52*, 4623. [[CrossRef](#)]
31. Zinke-Allmang, M. Phase separation on solid surfaces: Nucleation, coarsening and coalescence kinetics. *Thin Solid Films* **1999**, *346*, 1–68. [[CrossRef](#)]
32. Loncaric, M.; Sancho-Parramon, J.; Zorc, H. Optical properties of gold island films—A spectroscopic ellipsometry study. *Thin Solid Films* **2011**, *519*, 2946–2950. [[CrossRef](#)]
33. Qian, H.; Xiao, Y.; Lepage, D.; Chen, L.; Liu, Z. Quantum electrostatic model for optical properties of nanoscale gold films. *Nanophotonics* **2015**, *4*, 413–418. [[CrossRef](#)]
34. Yakubovsky, D.I.; Arsenin, A.V.; Stebunov, Y.V.; Fedyanin, D.Y.; Volkov, V.S. Optical constants and structural properties of thin gold films. *Opt. Express* **2017**, *25*, 25574. [[CrossRef](#)]
35. Meiklejohn, W.H.; Bean, C.P. New Magnetic Anisotropy. *Phys. Rev.* **1957**, *105*, 904. [[CrossRef](#)]
36. Gomoyunova, M.V.; Grebenyuk, G.S.; Pronin, I.I. Formation of ultrathin magnetic cobalt films on the Si(111)7 × 7 surface. *Tech. Phys.* **2011**, *56*, 865–868. [[CrossRef](#)]
37. Katmis, F.; Lauter, V.; Nogueira, F.S.; Assaf, B.A.; Jamer, M.E.; Wei, P.; Satpati, B.; Freeland, J.W.; Eremin, I.; Heiman, D.; et al. A high-temperature ferromagnetic topological insulating phase by proximity coupling. *Nature* **2016**, *533*, 513–516. [[CrossRef](#)]
38. Mogi, M.; Nakajima, T.; Ukleev, V.; Tsukazaki, A.; Yoshimi, R.; Kawamura, M.; Takahashi, K.S.; Hanashima, T.; Kakurai, K.; Arima, T.H.; et al. Large Anomalous Hall Effect in Topological Insulators with Proximitized Ferromagnetic Insulators. *Phys. Rev. Lett.* **2019**, *123*, 016804. [[CrossRef](#)] [[PubMed](#)]
39. Cortie, D.L.; Lin, K.W.; Shueh, C.; Hsu, H.F.; Wang, X.L.; James, M.; Fritzsche, H.; Bruck, S.; Klose, F. Exchange bias in a nanocrystalline hematite/permalloy thin film investigated with polarized neutron reflectometry. *Phys. Rev. B* **2012**, *86*, 054408. [[CrossRef](#)]
40. Saoudi, M.; Fritzsche, H.; Nieuwenhuys, G.J.; Hesselberth, M.B.S. Size Effect in the Spin Glass Magnetization of Thin AuFe Films as Studied by Polarized Neutron Reflectometry. *Phys. Rev. Lett.* **2008**, *100*, 057204. [[CrossRef](#)]
41. Ankner, J.F.; Majrzak, C.F.; Homma, H. Magnetic dead layer in Fe/Si multilayer: Profile refinement of polarized neutron reflectivity data. *J. Appl. Phys.* **1993**, *73*, 6436. [[CrossRef](#)]
42. Dyadkina, E.A.; Grigoriev, S.V.; Lott, D.; Sitnikov, A.V.; Kalinin, Y.E. Study of the [(Co<sub>45</sub>Fe<sub>45</sub>Zr<sub>10</sub>)<sub>x</sub>(Al<sub>2</sub>O<sub>3</sub>)<sub>100-x</sub>/a-Si:H]<sub>m</sub> multilayer nanostructure by polarized neutron reflectometry. *Phys. B* **2011**, *406*, 2397–2400. [[CrossRef](#)]

43. Dyadkina, E.A.; Grigoryeva, N.A.; Vorobiev, A.A.; Grigoriev, S.V.; Lutsev, L.V.; Zhernenkov, K.; Wolff, M.; Lott, D.; Stognij, A.I.; Novitskii, N.N.; et al. Polarized neutron reflectometry from the interface of the heterostructures SiO<sub>2</sub>(Co)/Si and SiO<sub>2</sub>(Co)/GaAs. *Phys. B* **2009**, *404*, 2547–2549. [[CrossRef](#)]
44. Lutsev, L. *Magnetoresistance: Types, Roles and Research*; Gonzalez, R., Ed.; Nova Science Publishers, Incorporated: New York, NY, USA, 2017; pp. 65–121.
45. Fan, Z.; Li, P.; Zhang, L.; Mi, W.; Jiang, E.; Bai, H. Electrical transport properties and room-temperature positive magnetoresistance of Fe<sub>3</sub>O<sub>4</sub>/a-C/n-Si junctions. *Thin Solid Films* **2012**, *520*, 3641–3646. [[CrossRef](#)]
46. Volkov, N.; Tarasov, A.; Eremin, E.; Baron, F.; Varnakov, S.; Ovchinnikov, S. Extremely large magnetoresistance induced by optical irradiation in the Fe/SiO<sub>2</sub>/p-Si hybrid structure with Schottky barrier. *J. Appl. Phys.* **2013**, *114*, 093903. [[CrossRef](#)]